

# Joint Reconstruction of the Activity and the Attenuation in PET by Diffusion Posterior Sampling: a Feasibility Study

Clémentine Phung-Ngoc<sup>1</sup>, Alexandre Bousse<sup>1</sup>, Antoine De Paepe<sup>1</sup>, Hong-Phuong Dang<sup>3</sup>, Olivier Saut<sup>2</sup>, and Dimitris Visvikis<sup>1</sup>

<sup>1</sup>Univ. Brest, LaTIM, INSERM, UMR 1101, 29238 Brest, France.

<sup>2</sup>INRIA Monc, Université de Bordeaux, Bordeaux INP, CNRS.

<sup>3</sup>IETR - UMR CNRS 6164, CentraleSupélec Rennes Campus, 35576 Cesson-Sevigné, France.

**Abstract** This study introduces a novel framework for joint reconstruction of the activity and the attenuation (JRAA) in positron emission tomography (PET) using diffusion posterior sampling (DPS). By leveraging diffusion models (DMs), this approach directly addresses activity–attenuation dependencies, mitigating crosstalk issues prevalent in non-time-of-flight (TOF) settings. Experimental evaluations, conducted using 2-dimensional (2-D) XCAT phantom data, demonstrate that DPS significantly outperforms traditional maximum likelihood activity and attenuation (MLAA) methods, producing consistent and high-quality reconstructions even in the absence of TOF information. Ongoing work aims to extend our method to real 3-dimensional (3-D) data with encouraging preliminary findings.

## Introduction

Positron emission tomography (PET) plays a critical role in medical imaging such as in oncology and cardiology. For accurate quantification, PET imaging requires attenuation correction, typically achieved using complementary modalities like computed tomography (CT) or magnetic resonance imaging (MRI). However, these additional scans increase radiation exposure and the complexity of the imaging workflow.

To mitigate radiation dose—especially in scenarios such as follow-up studies or potential screening protocols—it is desirable to perform PET acquisition in a low-dose setting. A promising approach to achieve this is to derive the attenuation correction directly from the PET emission data with joint reconstruction of the activity and the attenuation (JRAA) techniques. Methods like maximum likelihood activity and attenuation (MLAA) have demonstrated reasonable success in time-of-flight (TOF) PET settings by simultaneously estimating activity and attenuation using [1] or by joint estimation of the activity and attenuation coefficients (ACs) [2–4]. However, these methods struggle in non-TOF PET scenarios due to activity–attenuation crosstalk.

Recent advances in deep learning (DL) have opened new possibilities for enhancing PET reconstruction. Techniques leveraging DL can predict attenuation-corrected images from non-corrected data or directly generate attenuation maps [5].

In parallel, diffusion models (DMs) have emerged as a powerful tool for solving inverse problems through diffusion posterior sampling (DPS) [6]. These approaches have demonstrated promising performance in medical imaging tasks [7] and more particularly in PET reconstruction [8, 9].

In this paper, we propose a novel framework for JRAA directly from PET emission data using DPS. Our approach extends the MLAA algorithm by integrating the joint prior probability distribution function (PDF) of the activity and attenuation maps derived through DPS.

Section 2 introduces the forward model, the inverse problem, the DPS approach from [6] and its integration into an MLAA-

like framework. Section 3 presents experimental results using the XCAT phantom [10] for both TOF and non-TOF data. Section 4 discusses the limitations of our method and potential avenues for future research. Section 5 concludes the paper.

## 2 Materials and Methods

### 2.1 Background on Joint Activity and Attenuation Reconstruction

The task consists of retrieving an activity image (or volume)  $\boldsymbol{\lambda} = [\lambda_1, \dots, \lambda_m]^\top \in \mathcal{X} \triangleq \mathbb{R}_+^m$ ,  $m$  being the number of pixels (or voxels), from a collection of PET measurements  $\boldsymbol{y} = \{y_{i,k}\} \in \mathcal{Y} \triangleq \mathbb{R}^{n_l \times n_t}$  where  $y_{i,k}$  denotes the number of detected  $\gamma$ -photon pairs at the  $i$ th line of response (LOR) and  $k$ th time bin (for TOF PET),  $n_l$  and  $n_t$  being respectively the number of LORs and the number of time bins ( $n_t = 1$  in the non-TOF case). The counting process is modeled with a Poisson random PDF,

$$y_{i,k} \mid \boldsymbol{\lambda}, \boldsymbol{\mu} \sim \text{Poisson}(\bar{y}_{i,k}(\boldsymbol{\lambda}, \boldsymbol{\mu})) \quad (1)$$

where the expectation  $\bar{y}_{i,k}(\boldsymbol{\lambda}, \boldsymbol{\mu})$  depends on the activity image  $\boldsymbol{\lambda}$  to reconstruct as well as on the  $\gamma$ -photon attenuation map represented by an image  $\boldsymbol{\mu} = [\mu_1, \dots, \mu_m]^\top \in \mathcal{X}$ . Ignoring background effects such as scatter and random coincidences, a standard forward model is

$$\bar{y}_{i,k}(\boldsymbol{\lambda}, \boldsymbol{\mu}) \triangleq a_i(\boldsymbol{\mu}) \cdot \sum_{j=1}^m p_{i,k,j} \lambda_j \quad (2)$$

where  $p_{i,k,j}$  is the probability that an emission from voxel  $j$  is detected in  $(i, k)$  (taking into account the system’s geometry, resolution and sensitivity) and  $a_i(\boldsymbol{\mu})$  is the  $i$ th AC, given by the Beer-Lambert law as

$$a_i(\boldsymbol{\mu}) = e^{-[\mathbf{R}\boldsymbol{\mu}]_i}, \quad (3)$$

$\mathbf{R} \in \mathbb{R}^{n_l \times m}$  being the discrete Radon transform which computes line integrals along each LOR.

In multimodal imaging, the attenuation map  $\boldsymbol{\mu}$  can be derived from an anatomical image obtained from CT or MRI. The activity image  $\boldsymbol{\lambda}$  can then be reconstructed by solving the maximum *a posteriori* optimization problem

$$\max_{\boldsymbol{\lambda} \in \mathcal{X}} p(\boldsymbol{y} \mid \boldsymbol{\lambda}, \boldsymbol{\mu}) \cdot p(\boldsymbol{\lambda}) \quad (4)$$

where the conditional PDF  $p(\boldsymbol{y} \mid \boldsymbol{\lambda}, \boldsymbol{\mu})$  is given by (1) (assuming conditional independence of the measurements) and  $p(\boldsymbol{\lambda})$  is the prior distribution on  $\boldsymbol{\lambda}$ . Since  $p(\boldsymbol{\lambda})$  is unknown, it is typically

approximated by  $p(\boldsymbol{\lambda}) = \exp(-R(\boldsymbol{\lambda}))$  where  $R: \mathcal{X} \rightarrow \mathbb{R}^+$  is a convex regularizer which ideally promotes image smoothness while preserving edges, in which case (4) is a penalized maximum likelihood problem that can be solved by means of iterative algorithms [11].

When  $\boldsymbol{\mu}$  is not available, it can be jointly estimated with  $\boldsymbol{\lambda}$  from the emission data  $\mathbf{y}$  by solving

$$\max_{\mathbf{x} \in \mathcal{X}^2} p(\mathbf{y} | \mathbf{x}) \cdot p(\mathbf{x}) \quad (5)$$

where  $\mathbf{x} = (\boldsymbol{\lambda}, \boldsymbol{\mu})$  is the two-channel image comprising the activity and the attenuation. In absence of the prior  $p(\mathbf{x})$ , solving (5) corresponds to the MLAA problem which can be solved using an iterative algorithm [1]. However, the results are affected by the  $\boldsymbol{\lambda}$ - $\boldsymbol{\mu}$  crosstalk when the TOF resolution is too low. Moreover, this approach can only reconstruct the images up to a scaling factor due to the  $\bar{y}_{i,k}(\boldsymbol{\lambda}/c, \boldsymbol{\mu} - \log c) = \bar{y}_{i,k}(\boldsymbol{\lambda}, \boldsymbol{\mu})$  identity.

## 2.2 Joint Activity and Attenuation Reconstruction using Diffusion Posterior Sampling

JRAA can leverage the utilization of the PDF  $p(\mathbf{x})$  in (5) to take into account prior knowledge on the pair  $(\boldsymbol{\lambda}, \boldsymbol{\mu})$ . This PDF being unknown, we propose to sample  $\mathbf{x}$  from  $p(\mathbf{x}|\mathbf{y})$  using DPS [6]. In the following  $\mathcal{Z} = \mathcal{X} \times \mathcal{X}$  denotes the activity/attenuation map space.

In DMs, noise is incrementally added to an image  $\mathbf{x}_0$ , sampled from the training dataset with a PDF  $p^{\text{data}}$ , through a diffusion process, resulting in a noisy image  $\mathbf{x}_t$  at each time step  $t = 1, \dots, T$ . The reverse process samples an image from a generalized version of  $p^{\text{data}}(\mathbf{x})$ , approximating the theoretical prior  $p(\mathbf{x})$ . We used the denoising diffusion probabilistic model (DDPM) [12] which samples  $\mathbf{x}_t$  given  $\mathbf{x}_{t-1}$  as

$$\mathbf{x}_t | \mathbf{x}_{t-1} \sim \mathcal{N}(\sqrt{\alpha_t} \mathbf{x}_{t-1}, (1 - \alpha_t) \mathbf{I}_{\mathcal{Z}}) \quad (6)$$

where  $\mathbf{I}_{\mathcal{Z}}$  is the identity matrix on  $\mathcal{Z}$  and  $\alpha_t$  is a scaling factor defined such that  $\mathbf{x}_T \sim \mathcal{N}(\mathbf{0}_{\mathcal{Z}}, \mathbf{I}_{\mathcal{Z}})$ . An approximate reverse process, involving the score function  $\mathbf{s}_t(\mathbf{x}_t, t) \triangleq \nabla \log p_t(\mathbf{x}_t)$ — $p_t$  being the PDF of  $\mathbf{x}_t$ —can be derived to compute  $\mathbf{x}_{t-1}$  from  $\mathbf{x}_t$  as

$$\begin{aligned} \mathbf{x}_{t-1} &= \frac{\sqrt{\alpha_t}(1 - \bar{\alpha}_{t-1})}{1 - \bar{\alpha}_t} \mathbf{x}_t + \frac{\sqrt{\bar{\alpha}_{t-1}}\beta_t}{1 - \bar{\alpha}_t} \hat{\mathbf{x}}_0(\mathbf{x}_t) + \sigma_t \mathbf{z} \\ \mathbf{z} &\sim \mathcal{N}(\mathbf{0}_{\mathcal{Z}}, \mathbf{I}_{\mathcal{Z}}), \end{aligned} \quad (7)$$

where  $\bar{\alpha}_t = \prod_{s=1}^t \alpha_s$ ,  $\sigma_t = (1 - \alpha_t)(1 - \bar{\alpha}_{t-1})/(1 - \bar{\alpha}_t)$ ,  $\beta_t = 1 - \alpha_t$  and  $\hat{\mathbf{x}}_0(\mathbf{x}_t) \triangleq \mathbb{E}[\mathbf{x}_0 | \mathbf{x}_t]$  is given by Tweedie's formula:

$$\hat{\mathbf{x}}_0(\mathbf{x}_t) = \frac{1}{\sqrt{\bar{\alpha}_t}} (\mathbf{x}_t + (1 - \bar{\alpha}_t) \mathbf{s}_t(\mathbf{x}_t, t)) \quad (8)$$

The score function  $\mathbf{s}_t$  is unknown and therefore is approximated by a neural network (NN)  $\mathbf{s}_{\theta}: \mathcal{Z} \times [0, T] \rightarrow \mathcal{Z}$  trained by score matching as

$$\min_{\theta} \mathbb{E}_{t, \mathbf{x}_0, \epsilon} \left[ \|\mathbf{s}_{\theta}(\mathbf{x}_t, t) - \nabla_{\mathbf{x}_t} \log(p_t(\mathbf{x}_t | \mathbf{x}_0))\|_2^2 \right] \quad (9)$$

where  $\mathbf{x}_0 \sim p^{\text{data}}$ ,  $\epsilon \sim \mathcal{N}(\mathbf{0}_{\mathcal{Z}}, \mathbf{I}_{\mathcal{Z}})$  and  $\mathbf{x}_t = \sqrt{\bar{\alpha}_t} \mathbf{x}_0 + \sqrt{1 - \bar{\alpha}_t} \epsilon$ . An equivalent formulation for DDPMs can be to

predict the added noise  $\epsilon$  [12]. In the following, this analogous formulation is used and  $\mathbf{s}_{\theta}(\mathbf{x}_t, t)$  represents the NN trained on noise estimation.

DPS aims at solving an inverse problem by combining the prior PDF  $p(\mathbf{x})$  and the likelihood of the measurements  $p(\mathbf{y}|\mathbf{x})$ . It uses the conditional score  $\nabla_{\mathbf{x}_t} p_t(\mathbf{x}_t | \mathbf{y})$  to guide the reverse diffusion process in order to recover an image matching the measurements  $\mathbf{y}$ . The conditional score is given by the Bayes' formula as

$$\nabla_{\mathbf{x}_t} \log p(\mathbf{x}_t | \mathbf{y}) = \nabla \log p(\mathbf{x}_t) + \nabla_{\mathbf{x}_t} \log p(\mathbf{y} | \mathbf{x}_t). \quad (10)$$

There is no explicit relation between  $\mathbf{y}$  and  $\mathbf{x}_t$ , thus making the computation of  $p(\mathbf{y}|\mathbf{x}_t)$  intractable. Instead, the following approximation is commonly used:

$$\nabla_{\mathbf{x}_t} \log p(\mathbf{y} | \mathbf{x}_t) \simeq \nabla_{\mathbf{x}_t} \log p(\mathbf{y} | \hat{\mathbf{x}}_0(\mathbf{x}_t)). \quad (11)$$

The overall DPS process, which consists in alternating between sampling from  $\mathbf{x}_t$  using (7) and performing a gradient descent step using (11), is summarized in Algorithm 1.

---

### Algorithm 1 DPS for JRAA

---

**Require:**  $T, \mathbf{y}, \{\zeta_t\}_{t=1}^T, \{\xi_t\}_{t=1}^T, \{\sigma_t\}_{t=1}^T, \{\alpha_t\}_{t=1}^T$   
1:  $\mathbf{x}_T = (\boldsymbol{\lambda}_T, \boldsymbol{\mu}_T) \sim \mathcal{N}(\mathbf{0}_{\mathcal{Z}}, \mathbf{I}_{\mathcal{Z}})$   
2: **for**  $t = T$  **to** 1 **do**  
3:    $\hat{\mathbf{x}}_0 \leftarrow \frac{1}{\sqrt{\alpha_t}} (\mathbf{x}_t + \sqrt{1 - \bar{\alpha}_t} \mathbf{s}_{\theta}(\mathbf{x}_t, t))$   
4:    $\mathbf{z} \sim \mathcal{N}(\mathbf{0}_{\mathcal{Z}}, \mathbf{I}_{\mathcal{Z}})$   
5:    $\mathbf{x}'_{t-1} \leftarrow \frac{\sqrt{\alpha_t}(1 - \bar{\alpha}_{t-1})}{1 - \bar{\alpha}_t} \mathbf{x}_t + \frac{\sqrt{\bar{\alpha}_{t-1}}\beta_t}{1 - \bar{\alpha}_t} \hat{\mathbf{x}}_0 + \sigma_t \mathbf{z}$   
6:    $(\boldsymbol{\lambda}'_{t-1}, \boldsymbol{\mu}'_{t-1}) \leftarrow \mathbf{x}'_{t-1}$   
7:    $\boldsymbol{\lambda}_{t-1} \leftarrow \boldsymbol{\lambda}'_{t-1} + \zeta_t \nabla_{\boldsymbol{\lambda}_t} \log p(\mathbf{y} | \hat{\mathbf{x}}_0)$   
8:    $\boldsymbol{\mu}_{t-1} \leftarrow \boldsymbol{\mu}'_{t-1} + \xi_t \nabla_{\boldsymbol{\mu}_t} \log p(\mathbf{y} | \hat{\mathbf{x}}_0)$   
9:    $\mathbf{x}_{t-1} \leftarrow (\boldsymbol{\lambda}_{t-1}, \boldsymbol{\mu}_{t-1})$   
10: **end for**  
11: **return**  $\mathbf{x}_0$

---

## 3 Experiments

### 3.1 Training, Emission Data Simulation and Evaluation

All methods (training and reconstruction) were implemented with PyTorch.

We generated a collection of activity-attenuation pairs  $\mathbf{x} = (\boldsymbol{\lambda}, \boldsymbol{\mu})$  using the XCAT software [10] with different morphology and respiratory motion parameters to create a diverse dataset—without tumors included. The images consist of 2-dimensional (2-D)  $128 \times 128$  slices with a 3-mm pixel size. The image pairs were used as follows: 4,000 for training, 1,600 for validation and 10 for testing—training and testing slices were extracted from different phantoms. We solved the score-matching problem (9) using the Adam optimizer with approximately 250 epochs. The training was performed on standardized images, and the standardization was taken into account in the forward model (1).

We trained two score functions  $\mathbf{s}_{\theta}(\cdot, t): \mathcal{Z} \rightarrow \mathcal{Z}$ . The first score uses the proposed model and was trained on matching  $(\boldsymbol{\lambda}, \boldsymbol{\mu})$  pairs in order to account for dependencies between  $\boldsymbol{\lambda}$  and  $\boldsymbol{\mu}$  (referred to as DPS), while the second is of the form  $\mathbf{s}_{\theta}(\mathbf{x}, t) = [\mathbf{s}_{\phi}(\boldsymbol{\lambda}, t), \mathbf{s}_{\psi}(\boldsymbol{\mu}, t)]$ ,  $\theta = (\phi, \psi)$ , where the two score functions  $\mathbf{s}_{\phi}(\cdot, t), \mathbf{s}_{\psi}(\cdot, t): \mathcal{X} \rightarrow \mathcal{X}$  were trained independently on the

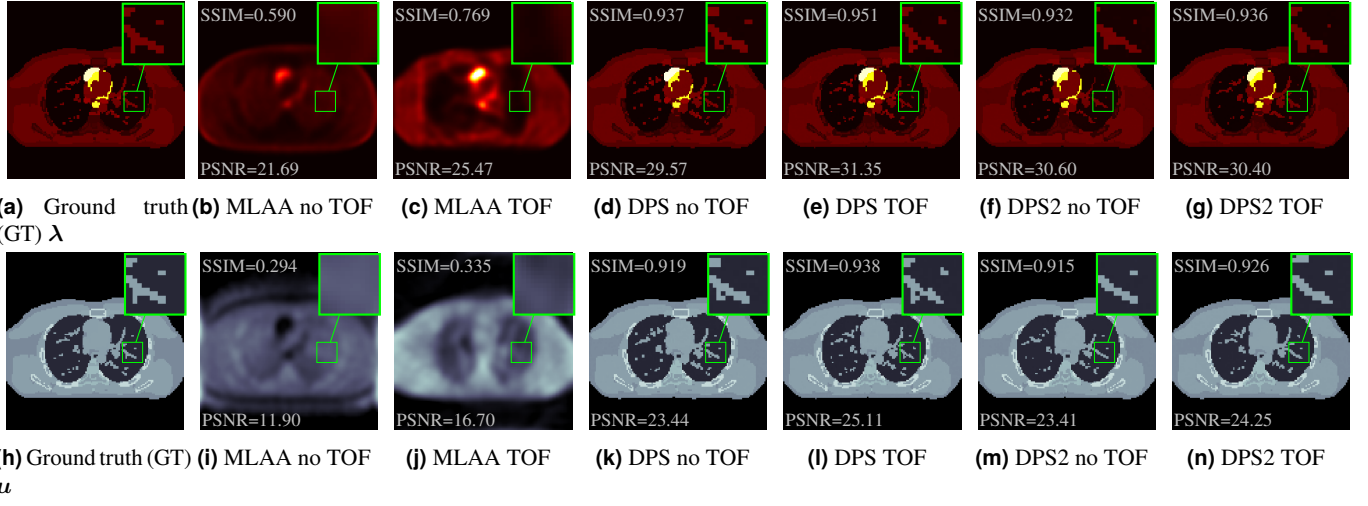


**Figure 1:** Ground truth (GT) and reconstructed images.

activity images and attenuation images respectively—this model assumes that  $\lambda$  and  $\mu$  are independent, i.e.,  $p(\mathbf{x}) = p(\lambda) \cdot p(\mu)$  (referred to as DPS2).

The emission raw data  $\mathbf{y}$  were generated following (1) using pairs  $\mathbf{x} = (\lambda, \mu)$  from the testing dataset. We generated TOF and non-TOF data using an homemade PET projector with a 5-mm full width at half maximum (FWHM) spatial resolution, a 60-mm FWHM temporal resolution and 315 projection angles. We used  $\tau = 5 \cdot 10^{-1}$  and we ignored background effects ( $\mathbf{r} = \mathbf{0}_y$ ).

The images were reconstructed using DPS, DPS2 as well as MLAA—with 50 outer iterations—for comparison. We used the peak signal-to-noise ratio (PSNR) and structural similarity index measure (SSIM)—with the ground truth (GT) images as references—as figures of merit, computed using the functions `peak_signal_noise_ratio` and `structural_similarity` from the Python package `skimage.metrics`.

### 3.2 Results

GT and reconstructed images are shown in Figure 1. MLAA-reconstructed images without TOF suffer from  $\lambda$ - $\mu$  crosstalk as expected, while MLAA with TOF does a reasonably good job although images suffer from noise amplification and partial volume effects due to the intrinsic resolution of the imaging system. On the other hand, DPS- and DPS2-reconstructed images achieve near perfect-resolution and noise-free reconstruction, even in absence of TOF data. In addition, we observe that DPS-reconstructed  $\lambda$  and  $\mu$  share similar features while some discrepancies can be observed with DPS2 (e.g., magnified area in the lungs).

Figure 2 shows SSIM vs PSNR plots of the DPS and DPS2 methods for the 10 testing data in the high-count setting—MLAA reconstructions were omitted for visibility as they are largely outperformed. We observe that DPS outperforms DPS2. More particularly, DPS without TOF outperforms DPS2 with TOF, suggesting that the reconstruction benefits of the dependencies between  $\lambda$  and  $\mu$ .

The near perfect results achieved by DPS and DPS2 may raise questions about potential over-fitting due to potential lack of diversity in the XCAT-generated training data. We therefore

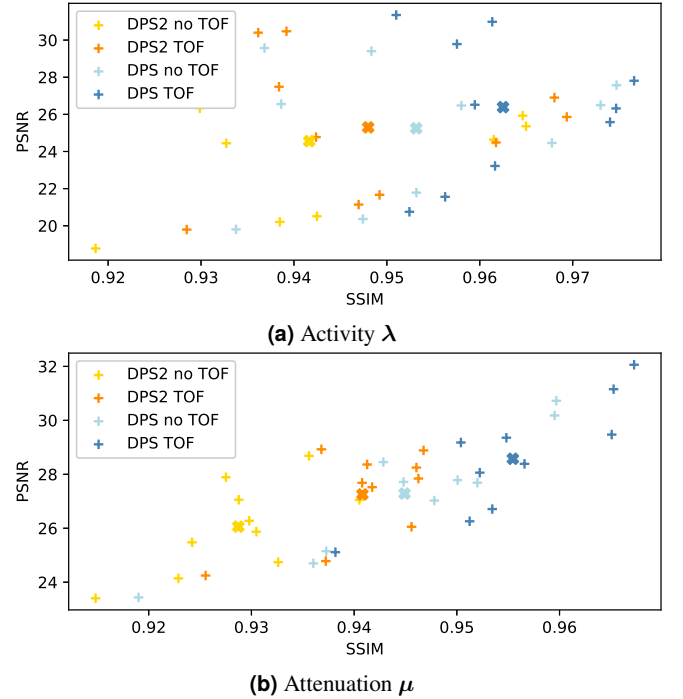


**Figure 2:** SSIM vs PSNR plots of the DPS and DPS2 methods for the 10 testing data. The bold crosses represent the mean SSIM and PSNR for each reconstruction method.

considered two out-of-distribution cases with a tumor in the lungs, illustrated in Figure 3(a), Figure 3(b) and Figure 3(g). The tumor takes the form of a uniform disk the first activity image (denoted  $\lambda$ ) and in the attenuation map (denoted  $\mu$ ), while it is modeled with a 2-D Gaussian kernel in the second activity image (denoted  $\lambda^*$ ). We then performed applied MLAA and DPS to the corresponding TOF data. In the first case, DPS is able to reconstruct the tumor in the activity and the attenuation (cf. Figure 3(e) and Figure 3(f)). In the second case, the DPS reconstruction is somehow capable of producing a “piecewise constant” tumor in the activity that mimics the Gaussian shape of the GT (cf. Figure 3(j) and profiles in Figure 4). This behavior results of the training on XCAT images which are piecewise constant. In addition, since the score was trained on matching image pairs, the reconstructed tumor in the attenuation map

inherits the same artifacts.

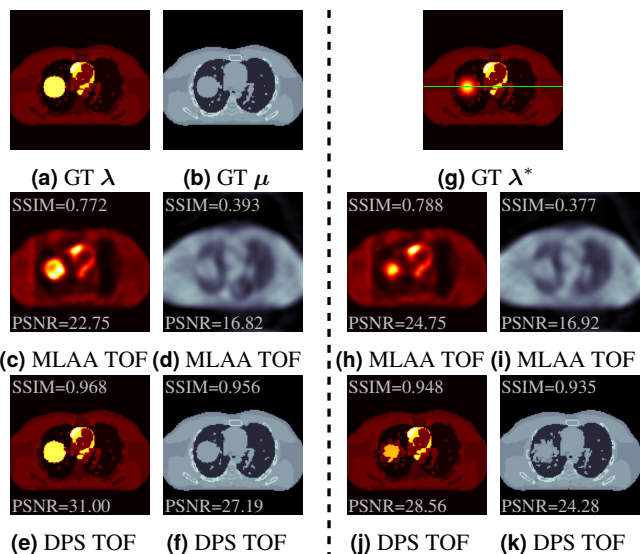


**Figure 3:** OOD reconstructions using MLAA and DPS, both with TOF, where the tumor in the GT activity images takes the form of a uniform disk and of a Gaussian function—the GT attenuation map  $\mu$  is identical in both scenarios.

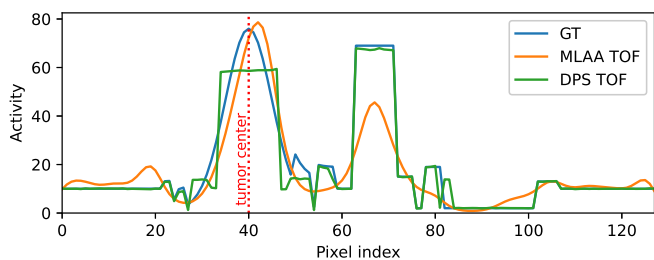


**Figure 4:** Activity profiles of out-of-distribution activity images. The profiles were drawn along the green line in Figure 3(g).

## 4 Discussion

The findings highlight the efficacy of DPS for JRAA in PET using emission data only, particularly in non-TOF settings where conventional methods often falter due to activity–attenuation crosstalk. Unlike MLAA, the DPS framework integrates prior knowledge through the learned joint PDF of activity and attenuation, ensuring consistency between the reconstructed images and effectively addressing crosstalk challenges. The experimental results confirm that DPS can generate high-quality, noise-free reconstructions, even under non-TOF conditions, and that it surpasses its independently trained variant, DPS2, by leveraging activity–attenuation dependencies. Similar observations were made in multi-energy CT reconstruction [13].

Nevertheless, this study acknowledges certain limitations. The models were exclusively trained on 2-D XCAT phantom data, which, despite their widespread use in simulation studies, lack the anatomical diversity and complexity of real-world patient datasets. This constraint potentially limits the generalizability of the model to clinical scenarios. Furthermore, the extension of this framework to 3-dimensional (3-D) volumes remains a critical next step. We are currently working on extending this method by incorporating real patient data and using data

compression techniques to handle 3-D data with encouraging results. These advancements are essential to validate the clinical applicability of DPS and to realize its potential in routine PET imaging workflows.

## 5 Conclusion

This study demonstrates the promise of DPS as an innovative tool for JRAA in PET imaging. By directly modeling the dependencies between activity and attenuation, DPS achieves superior performance, particularly in non-TOF scenarios. While the results represent a significant advancement over traditional MLAA methods, ongoing work aims to extend the approach to 3-D data and real-world clinical conditions with encouraging preliminary findings.

## Acknowledgment

This work was supported by the French National Institute of Health and Medical Research (Inserm), the French Institute for Research in Computer Science and Automation (Inria), the French National Research Agency (ANR) under grant No ANR-20-CE45-0020 and by France Life Imaging under grant No ANR-11-INBS-0006.

## References

- [1] A. Rezaei, M. Defrise, G. Bal, et al. “Simultaneous reconstruction of activity and attenuation in time-of-flight PET”. *IEEE transactions on medical imaging* 31.12 (2012), pp. 2224–2233. doi: [10.1109/NSSMIC.2011.6153883](https://doi.org/10.1109/NSSMIC.2011.6153883).
- [2] M. Defrise, A. Rezaei, and J. Nuyts. “Time-of-flight PET data determine the attenuation sinogram up to a constant”. *Physics in Medicine & Biology* 57.4 (2012), p. 885. doi: [10.1088/0031-9155/57/4/885](https://doi.org/10.1088/0031-9155/57/4/885).
- [3] A. Rezaei, M. Defrise, and J. Nuyts. “ML-reconstruction for TOF-PET with simultaneous estimation of the attenuation factors”. *IEEE transactions on medical imaging* 33.7 (2014), pp. 1563–1572. doi: [10.1109/TMI.2014.2318175](https://doi.org/10.1109/TMI.2014.2318175).
- [4] Y. Berker and Y. Li. “Attenuation correction in emission tomography using the emission data—a review”. *Medical physics* 43.2 (2016), pp. 807–832. doi: [10.1118/1.4938264](https://doi.org/10.1118/1.4938264).
- [5] X. Chen and C. Liu. “Deep-learning-based methods of attenuation correction for SPECT and PET”. *Journal of Nuclear Cardiology* 30.5 (2023), pp. 1859–1878. doi: [10.1007/s12350-022-03007-3](https://doi.org/10.1007/s12350-022-03007-3).
- [6] H. Chung, J. Kim, M. T. McCann, et al. “Diffusion posterior sampling for general noisy inverse problems”. In *Proceedings of the Eleventh International Conference on Learning Representations*. ICLR, 2023. doi: [10.48550/arXiv.2209.14687](https://doi.org/10.48550/arXiv.2209.14687).
- [7] G. Webber and A. J. Reader. “Diffusion models for medical image reconstruction”. *BJR| Artificial Intelligence* 1.1 (2024), ubae013. doi: [10.1093/bjra/ubae013](https://doi.org/10.1093/bjra/ubae013).
- [8] I. R. Singh, A. Denker, R. Barbano, et al. “Score-based generative models for PET image reconstruction”. *arXiv preprint arXiv:2308.14190* (2023). doi: [10.48550/arXiv.2308.14190](https://doi.org/10.48550/arXiv.2308.14190).
- [9] G. Webber, Y. Mizuno, O. D. Howes, et al. “Likelihood-Scheduled Score-Based Generative Modeling for Fully 3D PET Image Reconstruction”. *arXiv preprint arXiv:2412.04339* (2024). doi: [10.48550/arXiv.2412.04339](https://doi.org/10.48550/arXiv.2412.04339).
- [10] W. P. Segars, G. Sturgeon, S. Mendonca, et al. “4D XCAT phantom for multimodality imaging research”. *Medical physics* 37.9 (2010), pp. 4902–4915. doi: [10.1118/1.3480985](https://doi.org/10.1118/1.3480985).
- [11] A. De Pierro. “A modified expectation maximization algorithm for penalized likelihood estimation in emission tomography”. *IEEE Transactions on Medical Imaging* 14.1 (1995), pp. 132–137. doi: [10.1109/42.370409](https://doi.org/10.1109/42.370409).
- [12] J. Ho, A. Jain, and P. Abbeel. “Denosing diffusion probabilistic models”. *Advances in neural information processing systems* 33 (2020), pp. 6840–6851. doi: [10.48550/arXiv.2006.11239](https://doi.org/10.48550/arXiv.2006.11239).
- [13] C. Vazia, A. Bousse, B. Vedel, et al. “Diffusion posterior sampling for synergistic reconstruction in spectral computed tomography”. *2024 IEEE 21st international symposium on biomedical imaging (ISBI 2024)*. IEEE, 2024. doi: [10.1109/ISBI56570.2024.10635735](https://doi.org/10.1109/ISBI56570.2024.10635735).